

# Self- versus Directed- assembly of Nanoparticles via Pulsed Laser Induced Dewetting of Patterned Metal Films

J. D. Fowlkes<sup>1,\*</sup>, L. Kondic<sup>2</sup>, J. Diez<sup>3</sup>, Y. Wu<sup>4</sup>, and P. D. Rack<sup>1,4</sup>

1. Center for Nanophase Materials Sciences, Oak Ridge National Laboratory, Oak Ridge, Tennessee, 37831-6493, [fowlkesjd@ornl.gov](mailto:fowlkesjd@ornl.gov)

2. Department of Mathematical Sciences, Center for Applied Mathematics and Statistics, New Jersey Institute of Technology, Newark, New Jersey

3. Universidad Nacional del Centro de la Provincia de Buenos Aires (UNCBRA), Pinto 399, Tandil, Argentina

4. Materials Science and Engineering Department, The University of Tennessee, Knoxville, Tennessee, 37996-2200

**A nanoscale, synthetic perturbation was all that was required to nudge a natural, self-assembly process toward significantly higher order. Nanolithography was used to impose the perturbation which ultimately led to an organized *nanoparticle* array. Specifically, liquid-phase pulsed laser induced dewetting (PLiD) was used to transform metallic thin film strips into nanoparticle arrays. Initially, thin film strips retracted into fluid rivulets. Rivulet breakup followed, forming linear nanoparticle arrays via a process resembling the Rayleigh-Plateau (RP) instability; nanoparticle diameter and pitch were poorly controlled and disperse. We then demonstrated that the assembly accuracy and precision could be drastically improved by merely imposing a synthetic sinusoidal perturbation onto the lateral surfaces of the thin film strip. The synthetic perturbations in the strip translated into an unstable varicose oscillation on the rivulet during retraction – a precise nanoparticle diameter and pitch emerged thereby superseding the otherwise naturally evolving modes predicted by the modified Rayleigh-Plateau instability.**

Materials self-assembly predicated on easily defined initial conditions constitutes a groundbreaking demonstration of advanced materials synthesis. Nature provides the preeminent model of efficiency, parallel action and integration towards achieving complex, functional systems. The conversion of a simple input yielding a complex output is critical for natural systems. Taking a cue from natural systems, we have demonstrated a materials assembly method, based on nanofabrication, where a very simple input geometry (*a simple thin film strip*) was designed to produce a more complex output (*a precise, linear array of nanoparticles*) by making use of a naturally occurring instability, present in cylindrical fluid rivulets. Self-assembly was activated by pulsed laser induced dewetting (PLiD)<sup>1-8</sup>. Capillary forces initially drive the assembly through the large surface-to-volume ratio present in the thin film strip<sup>7</sup>. Concurrently,

the solid–liquid forces between the substrate and liquid rivulet stabilize the nanoparticle assembly<sup>9</sup>. *Moving one step further, an extremely sensitive switch was devised to direct the natural self–assembly process by designing an initial condition.* A nanoscale, synthetic sinusoidal perturbation imposed on the thin film strip edge led to an outstanding improvement in the precision and accuracy of the nanoparticle pitch and size relative to the freely propagating, natural fluid instability. The switch sensitivity proved ideal for directing assembly – slight, nanoscale changes in the initial sinusoid amplitude (~20nm) led to a drastic improvement in assembly fidelity.

Nanofabrication makes it possible to deposit materials systems that are far from equilibrium. Materials can be synthesized by physical vapor deposition and nanoscale lithography that have external geometries unachievable at thermal equilibrium. Such non–equilibrium materials rapidly re–organize into structures with fascinating spatial/morphological properties when subjected to brief yet high energy input.

Pulsed laser melting offers a unique opportunity to dictate materials assembly where rapid heating and cooling rates ( $10^{10}$ K/s) and nanosecond melt lifetimes are achievable. *Liquid lifetimes either less than, or on the order of, the self–assembly time–scale afford a unique opportunity to actively observe, engage and control the assembly process.* The SPEL (self–perfection by liquefaction) method provides a notable demonstration of the power of nanosecond, pulsed laser melting to refine nanoscale features and elements<sup>10</sup>. *Here, nanosecond PLiD was used to transform thin film metal strips with and without sinusoidal perturbations imposed on the boundaries into linear nanoparticle arrays by directing the natural evolution of a Rayleigh-Plateau (RP) liquid instability<sup>11-16</sup> modified by the solid substrate–liquid rivulet interaction.* The RP instability has been used previously to create nanostructures where both ion<sup>17</sup> and photon beams<sup>8,18</sup> were used to organize patterned metals. Xia et al. used periodicity engineering in the substrate to affect RP assembly<sup>8</sup>. In this work, we both engage and direct the RP instability by simply imposing a nanoscale perturbation the initial geometry of the thin film strip. Linear arrays of ordered, metallic nanoparticles are desirable for a number of nanotechnology applications including plasmon resonance waves<sup>19</sup>, nanomagnetism<sup>20,21</sup>, magnetic recording via plasmon antennas<sup>22</sup> and storage<sup>23</sup>.

Mechanistically, the patterned metal (Ni) strips are laser irradiated above their melt threshold, inducing the liquid phase retraction of the flat strips to a rivulet shape during the intermediate stages of the process; a static cylindrical fluid jet results, truncated along the jet axis by the substrate. On the rivulet, a range of varicose oscillations become unstable leading to the formation of droplets as the rivulet breaks up. *Without synthetic perturbations, the varicose modes<sup>8,18</sup> of wavelengths close to the most unstable one, characterized by the fastest growth rate for the rivulet geometry, ultimately sets the natural variation, i.e., dispersion, of the nanoparticle pitch and size.* In contrast, the precision achieved in nanoparticle size and spacing, accomplished by

imposing synthetic perturbations overwhelmingly exceeds that attainable by the natural RP-like destabilization process.

While there are differences in the driving forces that participate in the destabilization of a substrate-supported liquid rivulet (viscosity, capillary and liquid–solid interaction) compared with a free standing, Rayleigh-Plateau jet (inertial and capillary forces) as summarized by Diez et al<sup>9</sup>, we refer to the destabilization of a substrate supported rivulet as a modified Rayleigh-Plateau instability, since we have shown that the results of the two instability mechanisms are comparable for the nanoscale liquid metals studied here<sup>18,24</sup>. Notably, liquid phase self–assembly via the spinodal, or thin film instability,<sup>1-3,6,24-26</sup> has also been explored for a host of metallic materials where a similar disperse nanoparticle size and spacing distribution results as a consequence of the hydrodynamic evolution of the underlying instability. In addition, solid–state dewetting driven by surface diffusion<sup>27</sup> also leads to nanoparticle formation<sup>28-30</sup>.

We report here; (1) without synthetic perturbations, the rivulet destabilization into droplets can be understood based on the modified RP instability mechanism, leading to the formation of dispersed nanoparticles. (2) Synthetic nanoscale varicose perturbations, characterized by a length–scale larger than a critical wavelength lead to a drastic reduction in particle dispersion (as measured by the particle size and pitch of the final, organized structure). (3) Linear stability analysis (LSA) of the modified RP model correctly predicts the initial stages of the instability development as well as the critical wavelength required for synthetic perturbations to yield ordered structures. (4) Non-linear time-dependent simulations of hydrodynamic evolution reproduce detailed nanoscale spatial and temporal features observed during both liquid phase retraction and instability growth.

#### Brief methods: rivulet formation starting from thin, nanoscale metallic films

*The objective of our methodology is to precisely organize array of nanoparticles originating from the dewetting of a liquid rivulet. This, however, requires the creation of the semi-cylindrical rivulet which is difficult by standard nanolithography S1. Instead, a very thin film strip was deposited, which was designed to retract upon melting into the desired nanoscale rivulet geometry. Nanolithography (see Methods) along with physical vapor deposition was used to define metallic (nickel, Ni) thin film strips with both straight (figure 1a) and sinusoidal edges (shown later). The cross–sectional area of the thin film strip was designed to contract into a truncated liquid rivulet of radius ( $R_o$ ) according to the following area balance;*

$$h \times w = \theta R_o^2 - R_o^2 \sin \theta \cos \theta \quad (1)$$

where  $\theta$  is the equilibrium contact angle between the liquid Ni rivulet and silicon substrate. The angle  $\theta_o$  is dictated by the Young-Laplace equation. The rivulet

morphology (figure 1b) results from the conversion of the thin film strip (figure 1a) into a liquid by nanosecond PLiD. The straight edged strips (figure 1a) were designed to self-assemble as governed by the modified RP instability.

*The brief liquid lifetime per pulse (7.5–14.9ns) produced during PLiD was on the same order of magnitude as both the fluid transport<sup>5,7</sup> and modified RP instability timescales<sup>12,14,15,18,24</sup> which govern the rivulet self-assembly process and nanoparticle breakup, respectively.* This convergence of timescales, coupled with the rapid heating and cooling rates, made it possible to capture and visualize the temporal dynamics of the morphology evolution by repetitively pulsing and electron imaging (see **S2** for an example of a typical time-temperature plot)<sup>1</sup>.

### Nanoparticle self-assembly – derived from the evolution of the rivulet instability

*Destabilization of the rivulet morphology into a linear nanoparticle array begins with the growth of surface perturbation modes on the rivulet surface as shown in figure 1c.* The fastest growing modes ultimately out-pace slower ones, breaking up the rivulet into droplets which re-solidify. The resulting nanoparticle arrays exhibit a significant dispersion in nanoparticle radius and pitch<sup>8,18</sup>. Figure 1d-e show the growth rate ( $\omega$ ) versus wavelength ( $\lambda$ ) curve, *i.e.*, *dispersion curve*, estimated from both the standard RP theory of a fluid jet (blue solid line) as well as from the LSA based on the modified RP mechanism (*blue dashed lines*) for a Ni rivulet on a Si substrate with a radius of 1d)130±18 nm and 1e)165±9 nm. *Arriving at a desired nanoparticle size and pitch requires a detailed knowledge of the RP instability which dictates the assembly time and length scale<sup>8,18</sup>.* The modified RP mechanism gives a better prediction of the dispersion curve since substrate effects are considered. This can be seen in figures 1d–e by examining the position of dispersion curve maximum relative to the superimposed histogram of final nanoparticle pitch. In order to understand the origins of these instability mechanisms we briefly review both theories.

The RP model for a fluid jet predicts that varicose modes, characterized by the wavelength exceeding the critical one ( $\lambda_c$ ), evolve as a result of the interaction between transverse and transaxial pressure gradients in the fluid. Ignoring interaction with the substrate, one may consider that the pressure gradients arise in the liquid rivulet due to the presence of small oscillations on the rivulet surface. The growth rate of a perturbation of wavelength ( $\lambda=2\pi/k$ ), according to RP model is;

$$\omega^2 = \frac{\gamma}{\rho R_o} k R_o \frac{I_1(kR_o)}{I_0(kR_o)} (1 - k^2 R_o^2) \quad (2)$$

where  $\gamma$  is the liquid–vapor surface tension,  $\rho$  is the liquid density,  $k$  is the wavenumber and  $I_n(kR_o)$  are nth–order hyperbolic Bessel functions<sup>11,13,15</sup>. This expression predicts

that only the varicose surface modes of  $\lambda_c > 2\pi R_o$  are unstable and therefore yield droplets. The fastest growing mode satisfies  $\lambda_m \sim 9.02R_o$ .

The modified RP mechanism is derived by applying the lubrication approximation to model the evolution of a liquid rivulet *supported on a solid substrate*. The approach implemented here is based on lubrication approximation<sup>9</sup>, which yields the following equation;

$$3\mu \frac{\partial h}{\partial t} + \gamma \nabla \cdot (\mathcal{H}^3 \nabla \nabla^2 h) + \nabla \cdot [\mathcal{H}^3 \nabla \Pi(h)] = 0 \quad (3)$$

where  $h(x,y,t)$  is the Ni liquid thickness,  $\mu$  is the viscosity of liquid Ni and  $\Pi(h)$  represents the disjoining pressure which accounts for the interaction between rivulet and substrate. Linear stability analysis applied to equation (3) gives predictions for the evolution of small perturbations of the liquid rivulet surface; for simplicity we refer to the results of this model in the limit of small disturbances as 'LSA'. LSA predicts that the rivulet is stabilized by the presence of a substrate, where the extent of the stabilization is a function of the wetting angle of the fluid on the substrate<sup>9</sup>.

*Based on the modified RP mechanism, one expects the perturbations characterized by the growth rate close to the maximum ( $\lambda_m$ ) to be dominant.* Indeed, the final nanoparticle pitch is close to  $\lambda_m$ . This can be clearly gleaned from our experimental results in figure 1d showing the overlap of the nanoparticle pitch histogram and the LSA prediction. The resulting nanoparticle diameter is likewise set by the wavelength as well as by the initial rivulet radius.

Figures 1d-e demonstrate several characteristics of the LSA results (dashed lines): (1) negative growth rates for  $\lambda < 900\text{nm}$  ( $R_o = 130\text{nm}$ ) and  $\lambda < 1100\text{nm}$  ( $R_o = 165\text{nm}$ ) indicate stable varicose modes which ultimately decay on the rivulet surface favoring a smooth rivulet, i.e., no nanoparticle formation, (2) a maximum exists in the growth rate curve indicating a maximum growth rate of  $\omega = 5.2 \times 10^7 \text{s}^{-1}$  at  $\lambda_m = 1.45 \mu\text{m}$  ( $R_o = 130\text{nm}$ ) and  $\omega = 5 \times 10^7 \text{s}^{-1}$  at  $\lambda_m = 1.67 \mu\text{m}$  ( $R_o = 165\text{nm}$ ) and (3) the FWHM of the curves is disperse since  $\Delta\lambda \sim 1 \mu\text{m}$ . Importantly,  $\omega$  specifies approximately the time scale at which the formation of nanoparticles is expected ( $t_{\text{scale}} \sim 1/\omega \sim 20\text{ns}$ ), which is on the same order of magnitude as in experiments. *The fact that there is a whole range of wavelengths characterized by similar growth rates yields a significant variation in nanoparticle pitch (and size) for the self-assembly process.*

The statistical distribution of nearest-neighbor nanoparticle pitch was strongly correlated with the dispersion curve indicating that the modified Rayleigh-Plateau instability ultimately governs the PLiD self-assembly process. For example, the nanoparticle pitch histogram (*green curve, right ordinate*) shown in figure 1d for the

$R_0=130\text{nm}$  case overlaps well the LSA dispersion curve (left ordinate). This suggests close correlation of mode wavelength and nanoparticle pitch. In addition, the temporal evolution of perturbations prior to rivulet breakup was estimated from experiments by calculating the fast Fourier transform (FFT) of SEM images **S3** of rivulets. The FFT was found to provide an estimate of the amplitude distribution on the rivulet surface and could be directly compared to the dispersion curve. Remarkably, results indicated that (1) the final nanoparticle pitch is determined already at very early times, i.e., while perturbation amplitudes are of the order of 1-10nm, (2) the experimental data are slightly shifted to longer wavelengths relative to the RP prediction which is consistent with the stabilizing influence of the substrate (compare the red and two blue curves in figure 1c). Thus, the LSA estimate of dispersion dictated by the modified RP instability is found to accurately predict the dispersion of varicose modes observed experimentally.

#### Directed nanoparticle assembly: controlling the instability

Varicose perturbations characterized by a variety of wavelengths and amplitudes were lithographically patterned into the nickel thin film strips in order to explore the potential of directed-assembly to yield a very precise nanoparticle size and pitch. We refer to these modes as synthetic, in contrast to the naturally evolving modes which were shown above. Figure 2a demonstrates the as-synthesized nickel strips with a synthetic varicose perturbation for an average strip width of  $2\mu\text{m}$  and  $\lambda=1.96\mu\text{m}$  (*approximately the fastest growing mode as predicted by LSA, see figure 1e*) and various amplitudes. Below each strip we show the resultant morphology following PLiD using a fluence of  $420\text{mJ}/\text{cm}^2$  (5 pulses) which revealed striking results: 1) the synthetic mode is maintained with high-fidelity, through the liquid retraction phase of assembly, 2) the larger amplitude perturbations result in nanoparticles aligned at the peaks of the original synthetic perturbations and 3) rivulet pinch-off (as well as satellite droplets) occur at the perturbation troughs.

FFTs derived from the final dewetted morphologies were used to ascertain the effect of the initial perturbation amplitude (figure 2b). The zero initial amplitude experiments (green FFT) were effectively straight thin film strips. In this case, nanoparticle formation is ultimately governed by the LSA predicted instability as demonstrated previously. *By imposing a single wavelength, we effectively silence the thermally generated perturbations since the prescribed mode has a significant competitive advantage in terms of its initial amplitude.* The synthetic varicose perturbation effectively provides a “head start” for the amplitude evolution of an unstable mode – larger amplitudes lead to a more rapid formation of nanoparticles. Interestingly, this process hinges on the selection of an *unstable mode*. For example, the unstable  $1.96\mu\text{m}$  mode (figure 2b) both intensifies and sharpens with increasing amplitude as a high fidelity array of

nanoparticles emerges. *We have found that the FFT spectra closely mimic nanoparticle pitch histograms, with the FWHM of the distribution reflecting the variation in nanoparticle pitch.* Figure 2c shows clearly the narrowing of the pitch dispersion, i.e., a smaller FWHM, for *PLiD directed–assembly* ( $A_0=216\text{nm}$ , blue line) compared with the *PLiD self–assembly* results ( $A_0=0\text{nm}$ , green line). These Fourier spectra have been normalized to compare the FWHM of the respective curves.

The wavelength dependence of the synthetic perturbation evolution was studied by patterning thin film strips with *unstable* wavelengths ( $1.352$  and  $1.96\mu\text{m}$ ). By keeping the average strip width constant, the results could be compared with the results for unpatterned strips previously shown in figure 1e. In addition, a *stable* wavelength ( $\lambda=800\text{nm}$ ) exhibiting a negative growth rate was also explored. *Synthetic perturbations of stable wavelengths were found not to grow, even if prescribed with very large initial amplitudes.* Figure 3 summarizes the results for these experiments. Figure 3a shows SEM images of three distinct varicose perturbations where the amplitude ( $108\text{nm}$ ) and fluence were fixed. This produces a nearly constant liquid lifetime across the experimental set. As expected, the faster growing wavelength of the subset ( $1.96\mu\text{m}$  as predicted by LSA, figure 1e) is transformed into nanoparticles with a pitch reflecting the prescribed wavelength, whereas the relatively slower growing mode ( $1.352\mu\text{m}$ ) has only begun to break up. Remarkably, the stable varicose perturbation ( $800\text{nm}$ ) has decayed in amplitude favoring the transformation to a smooth rivulet. This result is consistent with the LSA results (figure 1e), which suggest negative growth rates below  $\lambda<1.1\mu\text{m}$ .

Figure 3b shows an SEM image collage of fifteen laser irradiated thin film strips (amplitude increasing from top–to–bottom in the figure) for the  $\lambda=1.352\mu\text{m}$  synthetic perturbation. Nanoparticles formed faster for larger initial amplitudes with a pitch reflecting the synthetic wavelength. Nanoparticles were less developed with decreasing amplitude. Oscillating, fragmented rivulets were observed for the smallest amplitudes. Figure 3c is a table summarizing the morphology for various combinations of wavelength and amplitude. *Consistent with our expectations, the table demonstrates that unstable wavelengths with larger growth rates require smaller synthetic amplitudes for discrete mode selection.* The nanoparticle formation timescale was consistent with the predictions of the LSA.

Longer liquid lifetimes (additional laser pulses) were required to observe the self–assembly for the *stable* varicose perturbation. Figure 3d shows a thin film annulus with an average synthetic wavelength of  $820\text{nm}$  (green feature) and the resultant nanoparticles (blue) overlaid on the original image. Annular films are convenient because they mitigate edge retraction effects (figure 1b) observed during the dewetting of strips<sup>24</sup>. The  $820\text{nm}$  mode is stable and does not reproduce the patterned wavelength. A dispersive nanoparticle size and pitch resulted which was consistent with

the evolution of the natural, disperse instability. The synthetic perturbation first decays leading to an apparently smooth, annular rivulet. This rivulet evolves into a nanoparticle array, as predicted by LSA, and not by the synthetic mode. This scenario is supported by a complementary control experiment **S4** which shows that the same distribution in nanoparticle pitch and size is obtained, whether or not the starting thin film annulus was smooth or patterned with a stable, synthetic 820nm mode. Conversely, the second annulus shown in figure 3d was synthetically perturbed by an *unstable* varicose wavelength (1.66 $\mu$ m). A remarkably precise nanoparticle size and pitch results following dewetting, which is consistent with the prescribed 1.66 $\mu$ m mode. Nanoparticle arrays are shown in figure 4 which exhibit the remarkable accuracy and precision in nanoparticle pitch/radius that results when PLiD directed assembly is carried out to completion.

To complement the experimental observations and predictions from LSA, fully non-linear 3-dimensional hydrodynamic simulations were performed **S5**. For brevity, we only show the consistency of the results with the experiments, as well as some new insights reached. Figure 5 shows the temporal evolution of the experimentally explored wavelengths of 800, 1352 and 1960nm for the synthetic perturbation amplitude of 108nm. For  $\lambda=1352$  & 1960nm, the distance between the dewetted nanoparticles corresponds to the prescribed wavelength as predicted by LSA, in agreement with the experiments (figure 3a). Also, the nanoparticle formation time scale is consistent, although slightly longer, than the time observed experimentally (figure 3a). The simulations capture even some subtle details of the experiments, such as the formation of satellite nanoparticles visible in the simulations for  $\lambda=1960$ nm and in the experiments in figure 2. In contrast, the short wavelength perturbation ( $\lambda=800$  nm) did not break up but rather formed a uniform rivulet on the timescale considered in figure 5a. However, at longer times, nanoparticles emerged with a pitch much larger than the prescribed 800nm perturbation. Additional imposed random perturbations characterized by a range of wavelengths and small random amplitudes prevailed and the resulting pitch was consistent with the linearly unstable wavelengths (figure 5b).

## Conclusions

Self- and directed- assembly of metallic nanoparticle arrays was accomplished by synthesizing nickel thin film structures far from equilibrium and initiating their assembly via pulsed laser melting. The modified Rayleigh-Plateau instability mechanism, including the effect of fluid-solid interaction, was found to faithfully describe the main features of the instability process, including the relevant time scales, where a fluid rivulet destabilized into an array of nanoparticles. Yet, the spacing between nanoparticles and the distribution of nanoparticle radii is unacceptably disperse for many practical applications. This variation in pitch and size resulted from the presence

of a multitude of unstable modes which randomly evolve on the rivulet surface. We engaged and directed the natural assembly process by prescribing “synthetic”, unstable modes in the starting thin film structure. The synthetic mode in the strip (a sinusoid located along the strip edges) translated into an unstable varicose oscillation on the rivulet. Rivulet breakup ensued. A precise, controlled nanoparticle size and pitch emerged thereby superseding the otherwise naturally evolving modes predicted by the modified RP instability. Linear stability analysis of the modified RP model predicted experimentally observed nanoparticle distributions for the self-assembly process and suggested the properties of synthetic perturbations leading to desired results. Nonlinear hydrodynamic simulations reproduced the nanoscale spatial/temporal features observed in the assembly process, captured in the re-solidified nanoparticle morphologies. Simulation predictions were accurate for both the naturally evolving self-assembly process as well as for the directed assembly method used to tailor the final nanoparticle size and pitch. While unstable modes could be synthetically selected; synthetic, stable modes decayed and natural mode selection by the RP instability ensued.

## **Methods**

### *Electron beam lithography*

Nickel thin film strips of micro- and nano-scale dimensions were defined on Si wafer substrates using electron beam lithography (EBL) followed by direct-current (DC) magnetron sputtering. Focused electron beam exposure at 10keV and 150pA was performed using an FEI Nova 600 microscope combined with Raith ELPHY Quantum pattern generation software. A poly(methyl methacrylate) (PMMA)-based, positive tone electron resist 495-A4 provided by Shipley was exposed for pattern definition. The PMMA resist was spin-coated on a Si wafer chip  $\sim 1\text{cm}^2$  in area at 4000 rpm for 60s. Spin coating was followed by a 2 minute,  $180^\circ\text{C}$  hot plate bake. An exposure dose of  $240\ \mu\text{C cm}^{-2}$  was required to completely expose the electron resist in order to produce well defined and nanoscale thin film strip edges capable of supporting lateral sinusoid oscillations with an amplitude ( $A_0$ ) of 20nm or greater. Pattern exposure was accomplished using the Raith software package coupled with an external electron beam blanker attached to the FEI Nova microscope. Feature dimensions for scanning electron exposure were contracted by 15% in order for design dimensions to be precisely replicated in the PMMA resist owing to the proximity effect where the superfluous exposure of resist occurs beyond the extent of the intended and scanned region. Each individual feature was exposed using an electron probe step size of 16nm and a dwell time per exposure pixel of  $4.1\ \mu\text{s}$  producing an electron probe exposure velocity of  $3.9\ \text{mm s}^{-1}$ . An exposure write-field size of  $100\ \mu\text{m} \times 100\ \mu\text{m}$  was used to expose a linear array of thin film strip features spaced apart uniformly on a square grid array, most often but not restricted to, a  $5\ \mu\text{m}$  pitch. The write-field size was geometrically calibrated prior

to exposure using a microfabricated checkerboard array of 10  $\mu\text{m}$  squares to accurately pattern the designed features (a so-called Chessy pattern Si chip provided by Raith®). 495–A4 resist development was carried out in a 1:3 methyl isobutyl ketone (MIBK): isopropyl alcohol (IPA) solution for 100 s followed by an IPA rinse that physically revealed the exposed patterns in the resist. The thin film strips were exposed completely down to the underlying silicon substrate, surrounded by unexposed resist. An 8s exposure of the Si chip to an oxygen plasma generated in a reactive ion etcher (100W capacitively coupled plasma,  $10\text{ cm}^3\text{ min}^{-1}$   $\text{O}_2$  flow and a pressure setting of 150mTorr) was implemented in order to remove any ancillary residual resist from the exposed regions. Metal was then deposited in the exposed pattern.

#### *DC sputter deposition*

An AJA International 200 DC magnetron sputter deposition system was used to deposit the Ni thin film strips. Sputter deposition was conducted using the constant power mode at 30W under a constant chamber pressure of 3mTorr Ar. A static pressure was maintained with a gas flow rate of  $25\text{ cm}^3\text{ min}^{-1}$ . The resulting sputter rate of Ni was  $5.8\text{ nm}\times\text{min}^{-1}$  for a target-to-substrate distance of  $\sim 5\text{ cm}$ . A wet, metal lift-off procedure was used to dissolve unexposed resist resulting in the lift-off of the unwanted metal layer surrounding the thin film strip features. The metal lift off procedure consisted of immersing the Si chip in acetone for  $\sim 5$  minutes. Finally each sample was rinsed in acetone followed by isopropyl alcohol and blown dry using with  $\text{N}_2$  gas to remove any remaining debris from the Si chip samples.

#### *Ultraviolet, pulsed laser irradiation*

A Lambda Physik LPX–305i, KrF excimer laser (248 nm wavelength), with a full-width-at-half-maximum pulse duration of  $\sim 18\text{ ns}$  was used to irradiate the Ni thin film strips. The beam emerging from the lasing cavity was directed to an optical bench that contained an aperture for trimming the incoming beam to its most uniform, central portions and to define an object for focusing the beam through a fused-silica lens onto the samples. All laser treatments reported in this paper were conducted in air. A photon fluence range of  $380\text{--}420\text{ mJ/cm}^2$  was explored to induce liquid phase, thin film dewetting and the number of pulses investigated ranged from 1, up to 20, laser pulses. One to three laser pulses at an energy density of  $420\text{ mJ cm}^{-2}$  were used to expose the features reported here. This laser fluence was adequate to melt both the Ni and Cu thin films as characterized by scanning electron microscopy (SEM).

#### *Thin film strip dimensions*

Thin film strips were patterned at two different strip widths of  $1.4\mu\text{m}$  and  $2.05\mu\text{m}$  (figure 1a) to realize a rivulet radius of 145 nm and 175 nm, respectively, according to equation (1). Rivulet radii of  $130\pm 18\text{ nm}$  and  $165\pm 9\text{ nm}$  (figure 1b) were measured following PLiD

demonstrating both (1) the validity of equation (1) for our retraction scheme and (2) minimal loss of Ni via evaporation or diffusion into the substrate.

### *Energy dispersive spectroscopy*

Energy dispersive spectroscopy (EDS) measurements were collected using an EDAX Apollo XL instrument, attached to a FEI Nova 600 dual ion/electron beam microscope, which was equipped with a 30mm<sup>2</sup> active detection area. An electron accelerating voltage of 10keV was used to excite X-ray emission in an image capture area of 256 x 200 pixels in order to create a Ni and Si composition map over a region-of-interest containing Ni rivulets, as well as Ni nanoparticles, in order to determine the Ni purity following PLiD. Negligible intermixing between the Si substrate and dewetted Ni was found which led to the conclusion that the rivulets and nanoparticles Ni. The pixel size during x-ray acquisition was 50nm. An accumulation number of 64 images were averaged to yield the final image EDS composition map. The dwell time per pixel per scan was 50μs. Nickel is represented as red in the two-dimensional EDS derived composition maps and silicon is represented in the green channel (figure 1g).

## **Supplementary Material**

### **Supplement 1**

The lithography and metallization methods used constrain the maximum thin film thickness that could be obtained for defining the initial thin film slices. Poor edge fidelity present in the slice edges following the metal lift-off step limited the maximum thin film thickness to approximately 30nm. Beyond h=30nm, the edge roughness approached a value greater than 20nm. Edge roughness on this order of magnitude could potentially translate to the liquid rivulet upon PLiD producing an undesired perturbation in the rivulet. As a result, the aspect ratio (height/width) for the initial varicose slices was limited to relatively small h/w ratios.

It is also important to note that such a small h/w ratio could have potentially left the liquid retraction step susceptible to, for example, instabilities of spinodal or even 'pearling' type discussed in some detail in reference <sup>18</sup> The successful formation of the rivulet morphology for the film thickness and thin film strip width combinations presented in this paper demonstrate a successful process niche located between lithography constraints and other destabilizing forces.

### **Supplement 2**

It has been demonstrated that the cumulative liquid lifetime ( $n\tau_L$ ) produced by multiple ( $n$ ) laser pulses yields the same morphology as a single laser pulse equal to the cumulative melt time<sup>1</sup>. Moreover, the rapid heating and cooling rates leave negligible time for morphological relaxation mechanisms such as diffusion, oxidation, etc. As a result, it was possible to image the dewetting dynamics at various stages during both the transport and instability growth stages by multiple iterations of laser pulsing and SEM imaging. As an example, figure 1c shows several images at an intermediate step in the self-assembly process where the rivulet morphology has developed and surface perturbations are evident on the rivulet surface.

The liquid lifetime controls the available hydrodynamic transport time per laser pulse, *defined here as the time during which the entire Ni thin film thickness is liquefied*, therefore excluding time periods of partial liquefaction. Simulations of the time-temperature evolution of a Ni thin film supported on a silicon substrate revealed liquid lifetimes of 7.5ns and 14.9ns when using a laser fluence of 380 mJ/cm<sup>2</sup> and 420 mJ/cm<sup>2</sup>, respectively (figure 1). The details of this simulation, based on<sup>4,31-33</sup> are described below

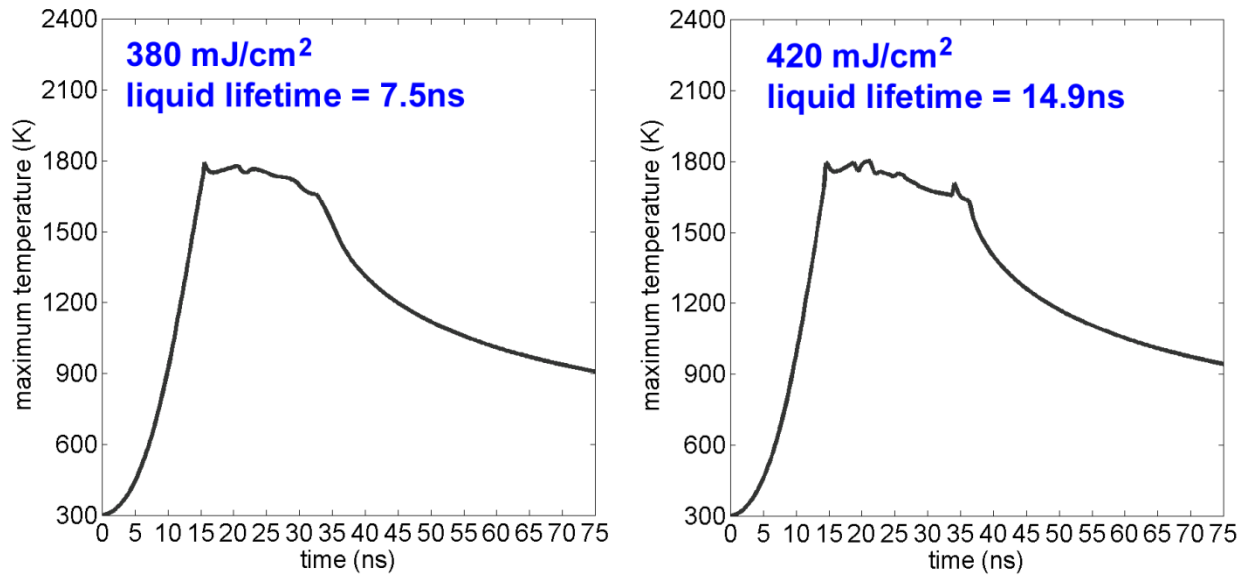


**Figure S2\_1** Liquid lifetime of the Ni thin film as a function of laser fluence.

The temperature profile in the nickel and silicon layers was estimated as a function of depth ( $z$ ) and time ( $t$ ) by simulating the one-dimensional heat equation, including a source term  $I(z,t)$  in order to account for the absorbed portion of the incident pulsed laser photon source;

$$\rho(z) \cdot c_p(z) \cdot \frac{\partial T(z,t)}{\partial t} = \frac{\partial}{\partial z} \cdot \left( k(z) \cdot \frac{\partial T(z,t)}{\partial z} \right) - I(z, t) \quad (5)$$

Material properties such as the density  $\rho(z)$ , heat capacity  $c_p(z)$  and thermal conductivity  $k(z)$  are represented with a  $z$ -dependence in equation (5) in order to account for material change across the nickel (Ni) thin film – silicon (Si) substrate boundary. Table 1 below lists the values of the variables mentioned in this Supplement. The source term included (1) a Gaussian approximation for the photon time pulse and considered (2) the liquid and solid phase reflectivity  $R(t)$  as well as the real refractive index ( $n$ ) and extinction coefficient ( $k$ ) of both the Ni and Si layers

$$I(z, t) = \frac{2 \cdot (1-R(t)) \cdot E_d(t) \cdot \alpha(z, t)}{\tau_{FWHM}} \cdot \sqrt{\frac{\ln 2}{\pi}} \cdot e^{-\alpha(z, t) \cdot z} \cdot e^{-\frac{4 \ln 2 \cdot (t-t_0)^2}{(\tau_{FWHM})^2}} \quad (6)$$

where  $E_d(t)$  is the time-dependent laser fluence ( $J/m^2$ ),  $\alpha(z, t)$  is the absorption coefficient (equation 7) and  $\tau_{FWHM}$  is the full width at half maximum of the laser pulse. The absorption coefficient is given as;

$$\alpha(z, t) = \frac{4\pi \cdot n \cdot k}{\lambda} \quad (7)$$

where  $\lambda$  is the laser wavelength. The reflectivity of either the solid or liquid phase may be derived from the real refractive index and the extinction coefficient by;

$$R(z = 0, t) = \frac{(n-1)^2 + k^2}{(n+1)^2 + k^2} \quad (8)$$

The velocity of the solid-liquid interface was estimated assuming that nucleation dynamics governed the speed of propagation<sup>31,33</sup> due to the rapid melting and resolidification processes that take place during nanosecond, pulsed laser irradiation. The interface velocity is dictated by the magnitude of the undercooling of the melt and/or overheating of the solid according to;

$$V(z, t)_i = V_o \cdot \left[ 1 - e^{-\frac{L(z)}{c_p \cdot T_m(z)} \frac{T_i(z, t) - T_m(z)}{T_i(z, t)}} \right] \quad (9)$$

where  $V_o$  is the interface limit velocity,  $L(z)$  is the latent heat of fusion,  $T_m(z)$  is the melting temperature,  $T_i(z, t)$  is the interface temperature and  $V(z, t)_i$  is the solid-liquid interface velocity. The phase change initiated at the Ni thin film surface and propagated into the simulation domain with time. The explicit finite difference method was used to estimate the time evolution of the temperature spatial profile. The stability criteria represented in equation (10) was maintained during the simulation

$$\frac{\Delta t \cdot k(z)_{max}}{c_p(z)_{min} \cdot \rho(z)_{min} \cdot \Delta z(z)_{min}} \leq 0.5 \quad (10)$$

where  $\Delta t$  is the simulation time step and  $\Delta z(z)$  is the depth dependent spatial discretization. A variable spatial grid size is used to increase efficiency. In the film

itself, we use small  $\Delta z_{surface}=1\text{nm}$ , Since the computational domain itself has to be relatively large in order to prevent the constant temperature boundary (300K) from affecting the solution, we use progressively larger  $\Delta z(z)$  as we move away from the surface, reaching the maximum value of 200nm at 25 microns below the solid/film interface. More precisely, the boundary conditions that we use are

$$\left. \frac{\partial T(0,t)}{\partial z} \right|_{z=h} = 0 \quad (11)$$

while within the silicon substrate the boundary condition is;

$$T(25\mu\text{m}, t) = 300\text{K} \quad (12)$$

Materials Properties				Laser & Simulation Properties		
	Si	Ni		$\lambda$	248	nm
k	150	90	J/m s K	$E_d$	380, 420	mJ/cm <sup>2</sup>
$c_p$	680	450	J/kg K	$\tau_{FWHM}$	18	ns
$\rho$	2300	7900	kg/m <sup>3</sup>	$t_o$	18	ns
L	1808	336	kJ/kg	$Z_{max}$	25	$\mu\text{m}$
$T_m$	1410	1453	K	$\Delta Z_{min}$	1	nm
$V_o$	312	500	m/s	$\Delta Z_{max}$	0.2	$\mu\text{m}$
n	1.5	(1.4,2.1)		$\Delta t$	2.5	fs
k	3.6	(2.1,3.3)		$t_{max}$	75	ns
				$T_o$	300	K
				$h_{Ni}$	23	nm

**Table 1** Ni and Si materials properties along with the pulsed laser heating simulation parameters. Entries in the table of the form (solid, liquid) represent the phase dependent values of specific properties.

### Supplement 3

Fast Fourier transforms (FFT) of SEM images were calculated by the following method. First, an SEM image of a partially fragmented rivulet was converted into binary format (rivulet=1, substrate=0). A summation was then calculated in the transaxial dimension of the resulting binary image (i.e. perpendicular to the cylindrical axis). The 1D FFT of the resulting data vector was then calculated. The resulting FFT was displayed as a spectrum of Fourier components ( $A_n$ ) vs. mode wavelength ( $\lambda$ ). The FFT was found to provide an estimate of the amplitude distribution on the rivulet surface and was directly compared to the modified Rayleigh–Plateau dispersion curve.

### Supplement 4

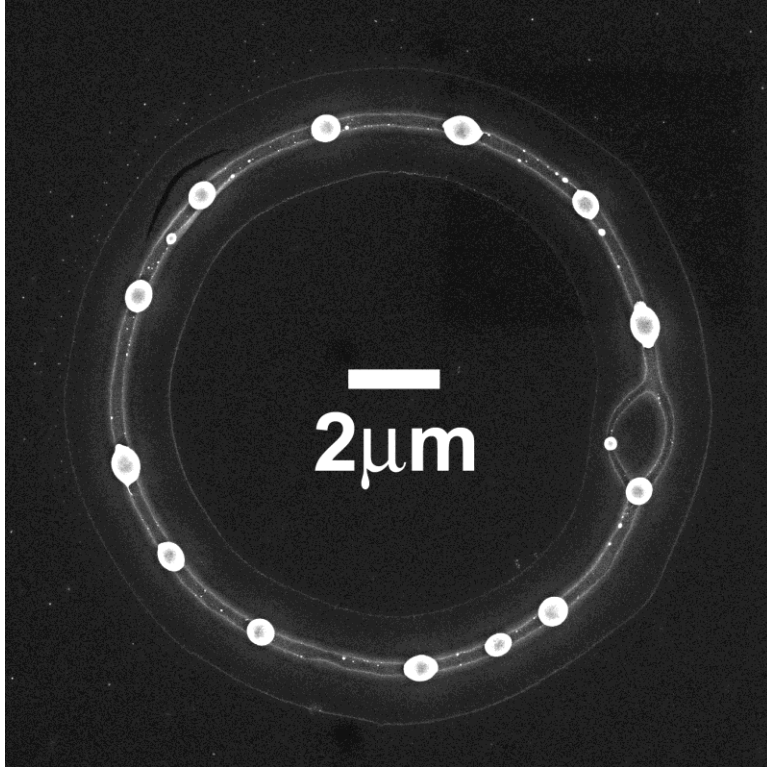


**Figure S4\_1** An SEM image of the nanoparticle morphology produced after the application of 20 laser pulses ( $E_d = 380 \text{ mJ/cm}^2$ ) to a smooth Ni annulus. The visible annular artifact in the image demarcates the outline of the thin film annulus prior to dewetting. The average pitch, as well as the standard deviation in pitch, are approximately the same as that obtained for a thin film annulus with a 820nm synthetic perturbation (see figure 3d).

### Supplement 5

The simulations are carried out by numerically solving the equation (3). The simulations are based on spatially discretizing the equation (3) using finite difference, and then carrying out the time evolution using the implicit Crank-Nicolson method, as described in detail elsewhere<sup>34</sup>. The initial condition is a thin film strip with smooth boundaries and periodic boundary conditions in the longitudinal direction. The initial thin film strip is then perturbed by varicose perturbations as discussed in the main text. The substrate itself is assumed to be pre-wetted by an ultrathin, equilibrium Ni film the thickness of which was determined by computing the value of Hamaker's constant based on a separate set of experiments involving breakup of a Ni film of uniform thickness as discussed in our earlier work<sup>24</sup>.

## References

- 1 Favazza, C., Kalyanaraman, R. & Sureshkumar, R. Robust nanopatterning by laser-induced dewetting of metal nanofilms. *Nanotechnology* **17**, 4229-4234 (2006).
- 2 Becker, J. *et al.* Complex dewetting scenarios captured by thin-film models. *Nat Mater* **2**, 59-63 (2003).
- 3 Seemann, R., Herminghaus, S. & Jacobs, K. Dewetting patterns and molecular forces: A reconciliation. *Phys Rev Lett* **86**, 5534-5537 (2001).
- 4 Koc, A. 3-D analysis of temperature distribution in the material during pulsed laser and material interaction. *Heat Mass Transfer* **40**, 697-706 (2004).
- 5 Rack, P. D., Guan, Y., Fowlkes, J. D., Melechko, A. V. & Simpson, M. L. Pulsed laser dewetting of patterned thin metal films: A means of directed assembly. *Appl Phys Lett* **92**, 223108 (2008).
- 6 Favazza, C., Trice, J., Krishna, H. & Kalyanaraman, R. Laser-induced patterning of Co nanostructures under ambient conditions. *Mater Res Soc Symp P* **890**, 153-158 (2006).
- 7 Fowlkes, J. D., Wu, Y. Y. & Rack, P. D. Directed Assembly of Bimetallic Nanoparticles by Pulsed-Laser-Induced Dewetting: A Unique Time and Length Scale Regime. *ACS Appl Mater Inter* **2**, 2153-2161 (2010).
- 8 Xia, Q. F. & Chou, S. Y. The fabrication of periodic metal nanodot arrays through pulsed laser melting induced fragmentation of metal nanogratings. *Nanotechnology* **20**, 285310 (2009).
- 9 Diez, J. A., Gonzalez, A. G. & Kondic, L. On the breakup of fluid rivulets. *Phys Fluids* **21**, 082105 (2009).
- 10 Chou, S. Y. & Xia, Q. F. Improved nanofabrication through guided transient liquefaction. *Nat Nanotechnol* **3**, 369-369 (2008).
- 11 Rayleigh, L. XVI. On the instability of a cylinder of viscous liquid under capillary force. *Philosophical Magazine Series 5* **34**, 145-154 (1892).
- 12 Brochard-Wyart, F. & Redon, C. Dynamics of Liquid Rim Instabilities. *Langmuir* **8**, 2324-2329 (1992).
- 13 Taylor, G. The Dynamics of Thin Sheets of Fluid .2. Waves on Fluid Sheets. *Proc R Soc Lon Ser-A* **253**, 296-312 (1959).
- 14 Sekimoto, K., Oguma, R. & Kawasaki, K. Morphological Stability Analysis of Partial Wetting. *Ann Phys-New York* **176**, 359-392 (1987).
- 15 Eggers, J. & Villermaux, E. Physics of liquid jets. *Rep Prog Phys* **71**, 036601 (2008).
- 16 Plateau, J. A. F. *Acad. Sci. Brux. Mem.* **16**, 3 (1843).
- 17 Lian, J., Wang, L. M., Sun, X. C., Yu, Q. K. & Ewing, R. C. Patterning metallic nanostructures by ion-beam-induced dewetting and Rayleigh instability. *Nano Lett* **6**, 1047-1052 (2006).
- 18 Kondic, L., Diez, J. A., Rack, P. D., Guan, Y. F. & Fowlkes, J. D. Nanoparticle assembly via the dewetting of patterned thin metal lines: Understanding the instability mechanisms. *Phys Rev E* **79**, 026302 (2009).
- 19 Van Orden, D., Fainman, Y. & Lomakin, V. Optical waves on nanoparticle chains coupled with surfaces. *Opt Lett* **34**, 422-424 (2009).
- 20 Bader, S. D. Colloquium: Opportunities in nanomagnetism. *Rev Mod Phys* **78**, 1-15, doi:DOI 10.1103/RevModPhys.78.1 (2006).
- 21 Chien, C. L., Zhu, F. Q. & Zhu, J. G. Patterned nanomagnets. *Phys Today* **60**, 40-45 (2007).
- 22 Stipe, B. C. *et al.* Magnetic recording at 1.5 Pb m<sup>(-2)</sup> using an integrated plasmonic antenna. *Nat Photonics* **4**, 484-488 (2010).

- 23 Rahman, M. T., Shams, N. N. & Lai, C. H. Nonlithographic fabrication of 25 nm magnetic nanodot arrays with perpendicular anisotropy over a large area. *J Appl Phys* **105**, 07C112 (2009).
- 24 Wu, Y., Fowlkes, J. D., Rack, P. D., Diez, J. A. & Kondic, L. On the Breakup of Patterned Nanoscale Copper Rings into Droplets via Pulsed-Laser-Induced Dewetting: Competing Liquid-Phase Instability and Transport Mechanisms. *Langmuir* **26**, 11972-11979 (2010).
- 25 Vrij, A. & Overbeek, J. T. Rupture of Thin Liquid Films Due to Spontaneous Fluctuations in Thickness. *J Am Chem Soc* **90**, 3074-3078 (1968).
- 26 Krishna, H., Favazza, C., Gangopadhyay, A. K. & Kalyanaraman, R. Functional nanostructures through nanosecond laser dewetting of thin metal films. *JOM* **60**, 37-42 (2008).
- 27 McCallum, M. S., Voorhees, P. W., Miksis, M. J., Davis, S. H. & Wong, H. Capillary instabilities in solid thin films: Lines. *J Appl Phys* **79**, 7604-7611 (1996).
- 28 Giermann, A. L. & Thompson, C. V. Solid-state dewetting for ordered arrays of crystallographically oriented metal particles. *Appl Phys Lett* **86**, 121903 (2005).
- 29 Kim, D., Giermann, A. L. & Thompson, C. V. Solid-state dewetting of patterned thin films. *Appl Phys Lett* **95**, 121903 (2009).
- 30 Lubber, E. J., Olsen, B. C., Ophus, C. & Mitlin, D. Solid-state dewetting mechanisms of ultrathin Ni films revealed by combining in situ time resolved differential reflectometry monitoring and atomic force microscopy. *Phys Rev B* **82**, 085407 (2010).
- 31 Hixson, R. S., Winkler, M. A. & Hodgdon, M. L. Sound Speed and Thermophysical Properties of Liquid-Iron and Nickel. *Phys Rev B* **42**, 6485-6491 (1990).
- 32 Bassler, B. T., Hofmeister, W. H., Carro, G. & Bayuzick, R. J. The Velocity of Solidification of Highly Undercooled Nickel. *Metall Mater Trans A* **25**, 1301-1308 (1994).
- 33 Zhang, Y. & Chen, J. K. Melting and resolidification of gold film irradiated by nano- to femtosecond lasers. *Appl Phys a-Mater* **88**, 289-297 (2007).
- 34 Diez, J. A. & Kondic, L. Computing three-dimensional thin film flows including contact lines. *J Comput Phys* **183**, 274-306, doi:DOI 10.1006/jcph.2002.7197 (2002).
- 35 Snoeijer, J. H., Le Grand-Piteira, N., Limat, L., Stone, H. A. & Eggers, J. Cornered drops and rivulets. *Phys Fluids* **19**, 042104 (2007).

## Acknowledgements

P Rack and J Fowlkes acknowledge support from the Material Sciences and Engineering Division Program of the DOE Office of Science (ERKCM38) for sponsoring the aspects of this work related to understanding the fundamental mechanisms operative during liquid phase, thin film dewetting. L Kondic, P Rack and J Fowlkes also acknowledge that the lithography and electron imaging results reported in this Article were conducted at the Center for Nanophase Materials Sciences, Oak Ridge National Laboratory and sponsored by the Scientific User Facilities Division (SUFD), Office of Basic Energy Sciences (BES), U. S. Department of Energy. L Kondic acknowledges support by the NSF grant No. [DMS-0908158](#). J Diez acknowledges CONICET-Argentina for travel support within the International Cooperation Program, and ANPCyT-Argentina for support within the project PID 2498/06.

**Figure 1:** Self assembly in the liquid phase by the modified Rayleigh–Plateau instability

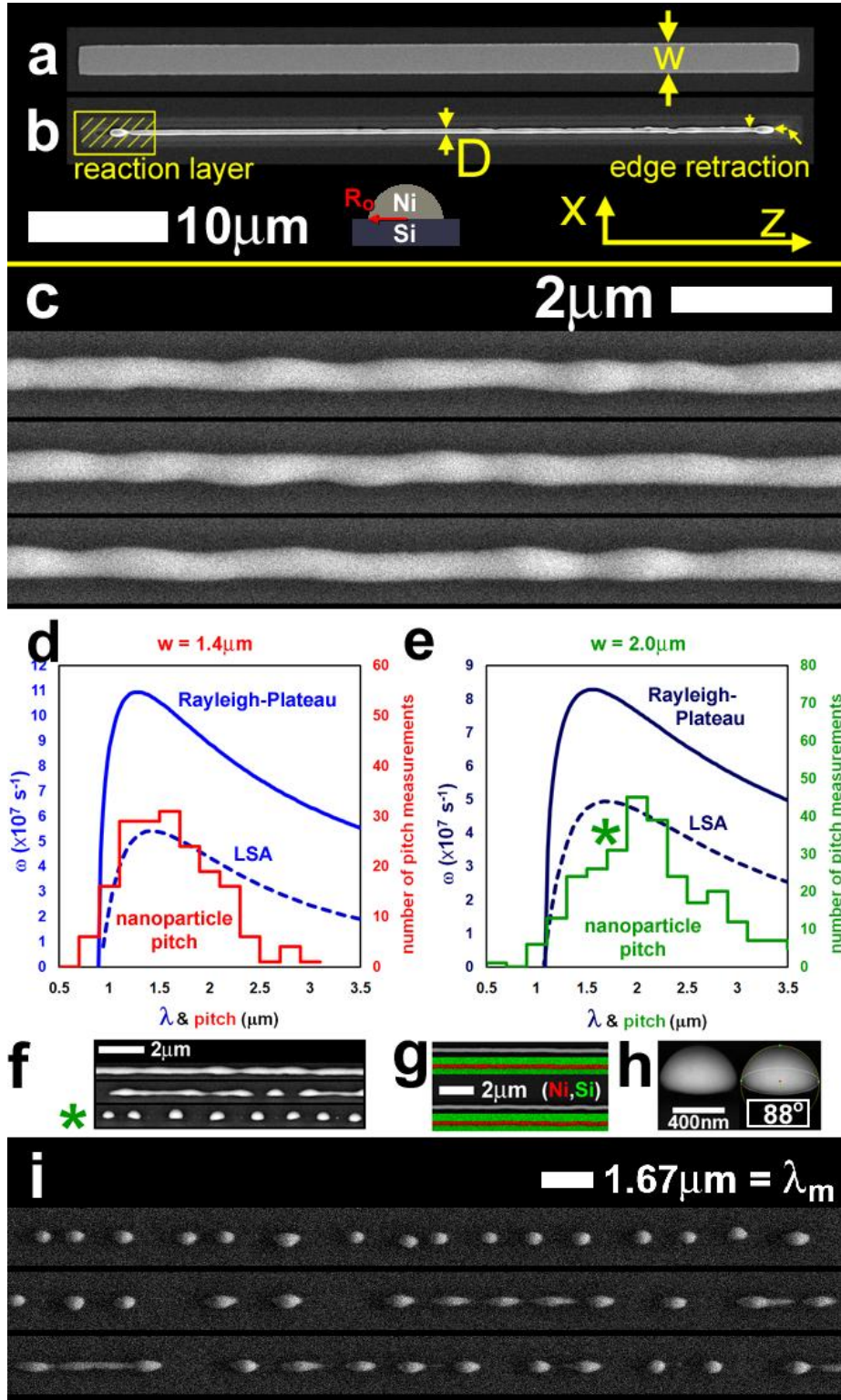
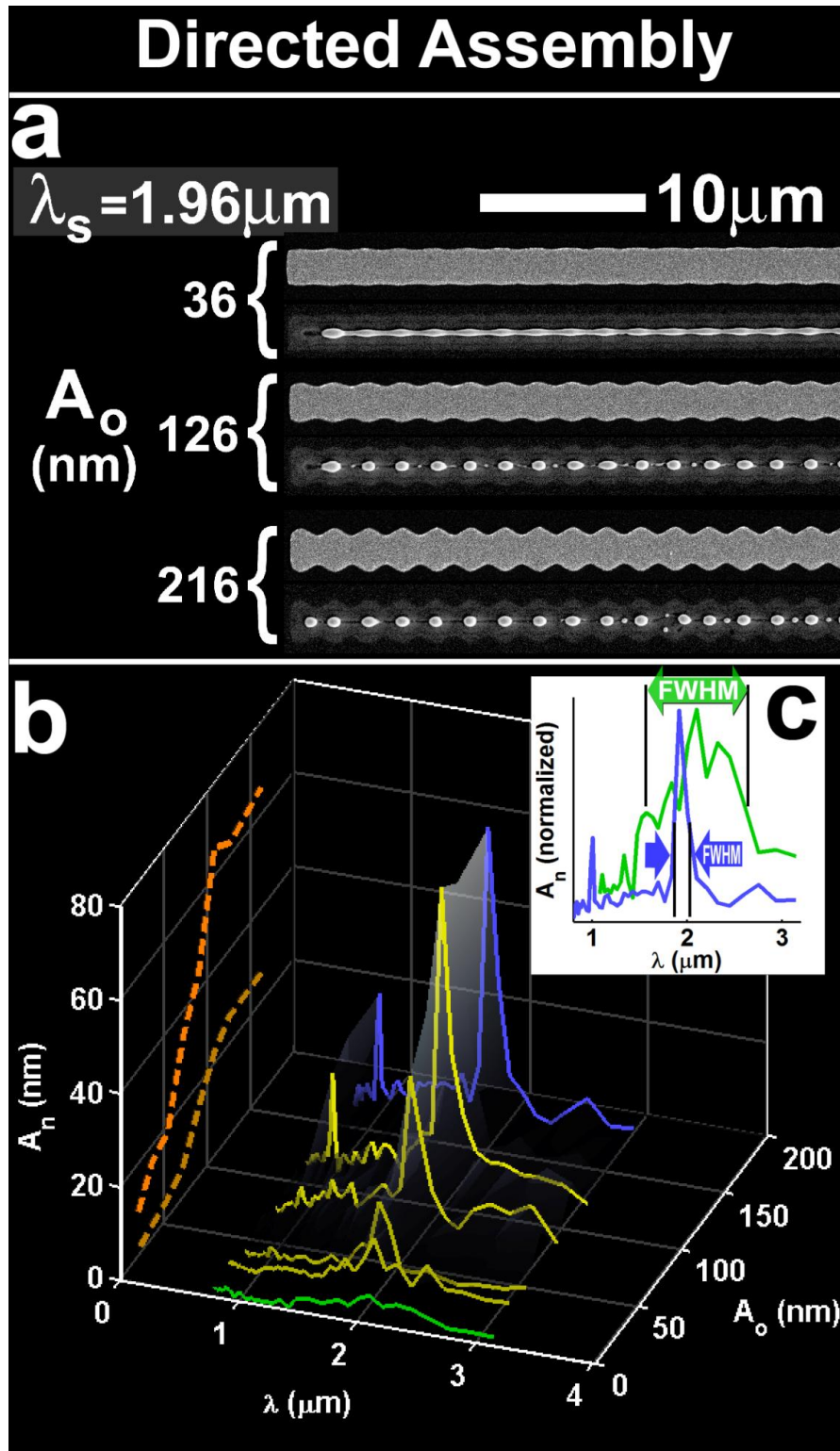
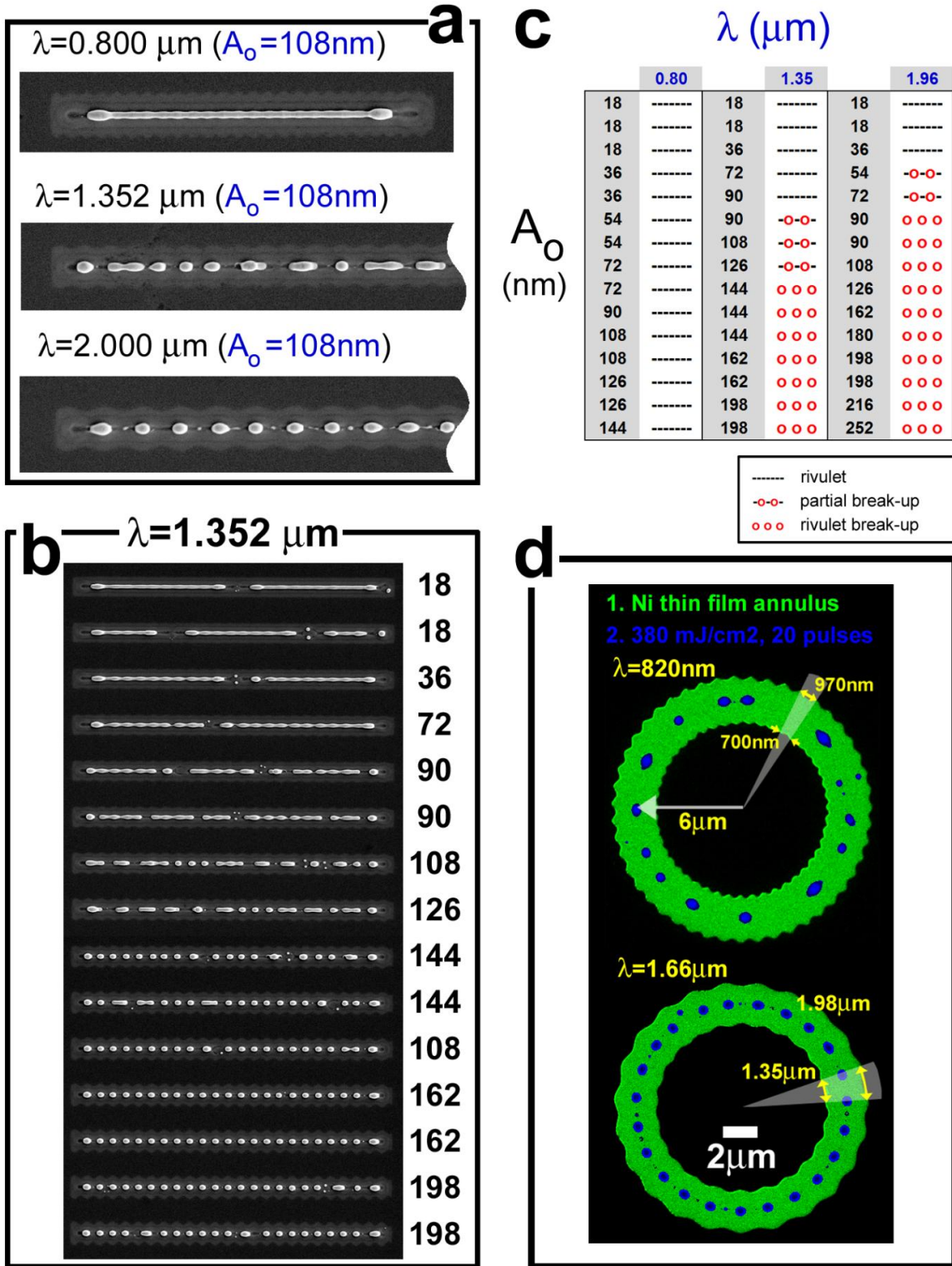


Figure 2: The transition from self- to directed assembly



**Figure 3:** Directed assembly by instability engagement using a nanoscale, synthetic perturbation



**Figure 4:** Directed assembly leads to the formation of high fidelity nanoparticle arrays

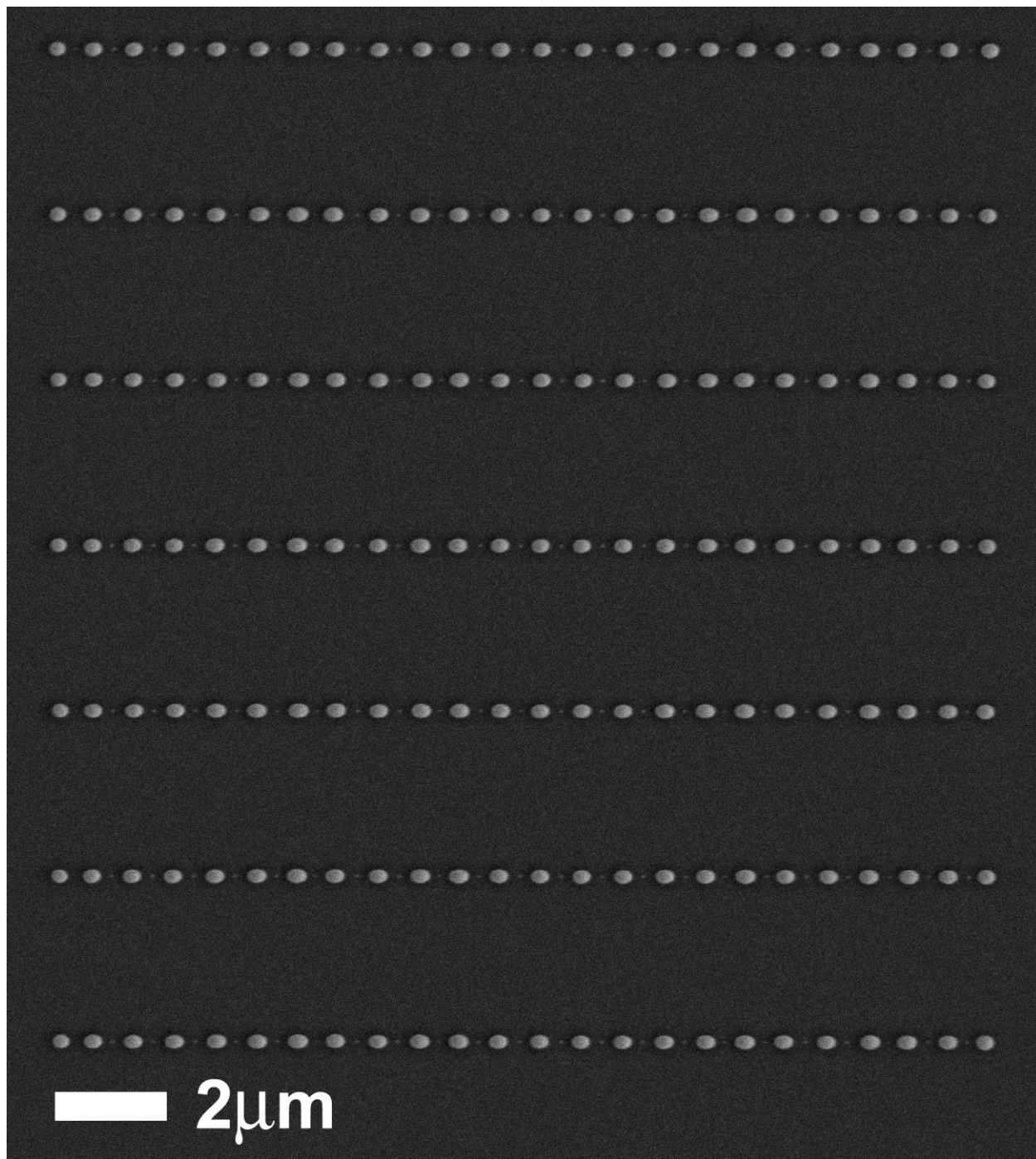
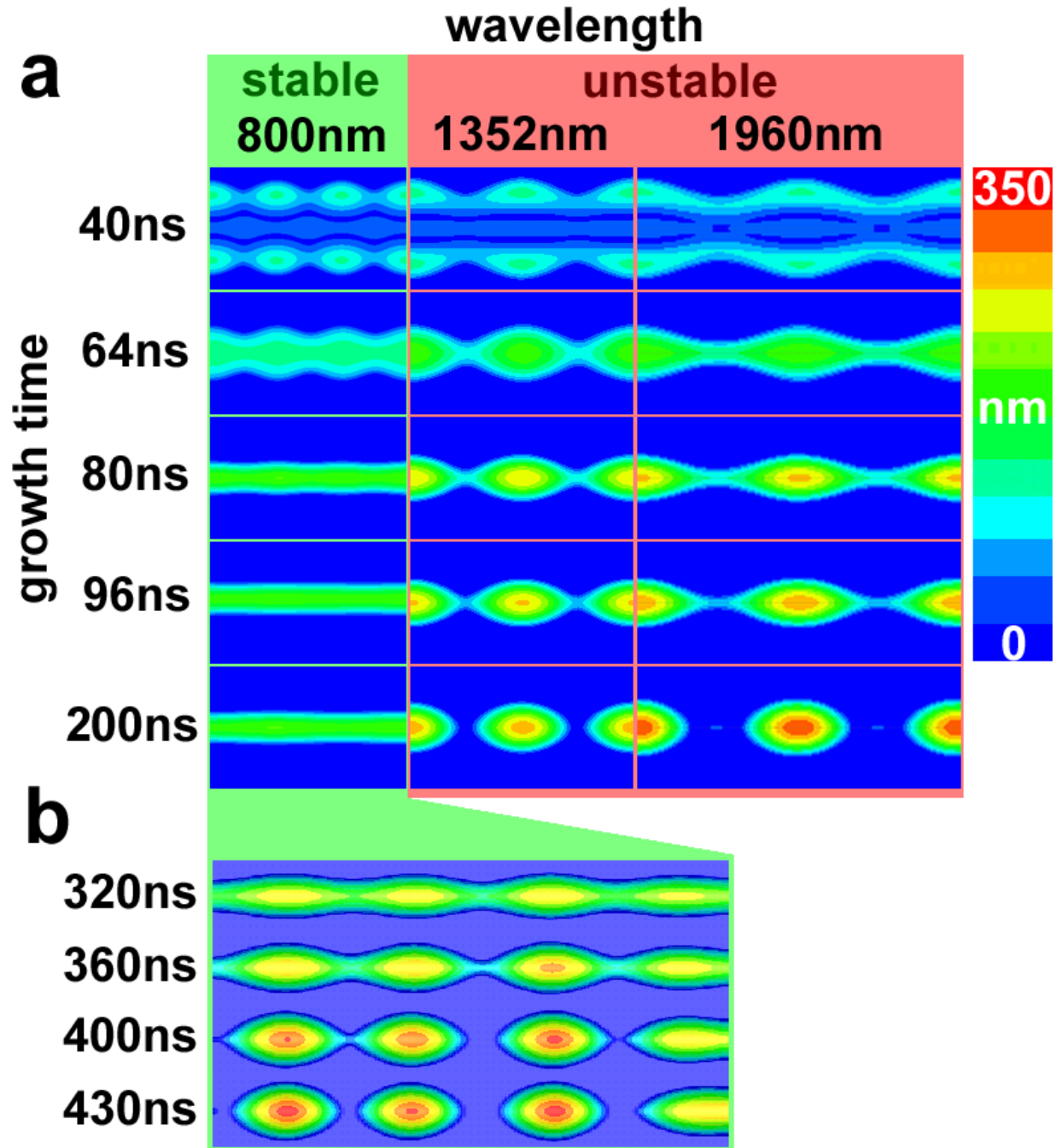


Figure 5: Directed assembly as predicted by non-linear hydrodynamic simulations



## Figure Legends

**Figure 1** The PLiD self assembly method starts by converting a thin film strip into a rivulet. a) An SEM image of a Ni thin film strip following electron beam lithography and metallization. The image was acquired normal to the Si substrate surface. The thin film strip dimensions were height ( $h$ ) =  $23\text{nm} \pm 1.2\text{nm}$ , width ( $w$ ) =  $2.05\mu\text{m}$  and a length of  $50\mu\text{m}$ . b) Strips rapidly transform, by fluid retraction, into a rivulet upon pulsed laser melting. A liquid rivulet with a radius ( $R_o$ ) of  $165\text{nm} \pm 9\text{nm}$  results following 5 KrF, 248nm laser pulses and an energy density of  $420\text{ mJ/cm}^2$  (liquid lifetime  $5 \times 14.9\text{ns} = 74\text{ns}$ ). An ultrathin reaction layer forms simultaneously during retraction which is presumably a very thin silicide ( $\text{Ni}_x\text{Si}_y$ ). This layer conveniently imprints the original strip dimension. Out-of-plane capillary forces drive the indicated (yellow arrows) edge and vertex retraction<sup>7,35</sup>. c) A modified Rayleigh–Plateau instability induces surface perturbations once the rivulet forms. In this case, the original thin film strip width ( $w$ ) was  $1.4\mu\text{m} \pm 18\text{nm}$ . A rivulet of  $R_o = 130\text{nm} \pm 18\text{nm}$  was formed following liquid phase retraction during 10 pulses of  $E_d = 380\text{ mJ/cm}^2$ . d–e) *Rivulet breakup occurs at varicose troughs. As a result, the final nanoparticle spacing distribution mirrors the dispersion curve ( $\omega$  vs  $\lambda$ ) which dictated its formation.* Linear stability analysis (LSA) based on the modified RP instability mechanism predicts the growth rate of unstable varicose perturbations as a function of their wavelength (*i.e.*, the dispersion curve) for the d) 130nm rivulet and e) 165nm rivulet as shown by the blue, hatched lines. The RP prediction for a free jet (without the effects of the substrate) is also shown (solid, blue lines). Histogram plots of the nearest-neighbor, nanoparticle spacing ( $R_o = 130\text{nm}$ , green histogram and  $R_o = 165\text{nm}$ , red histogram plot) reveal a strong correlation between the LSA predicted perturbation growth rate ( $\omega$ ) and final nanoparticle pitch. The pitch bin width for both histogram plots was 200nm. f) Tilted SEM images ( $\sim 45^\circ$ ) of the three stages of self-assembly for the  $R_o = 130\text{nm}$  rivulet; *top-to-bottom*, perturbations on the rivulet, partial rivulet breakup, and nanoparticle chain formation (the SEM image indicated by (\*)) is a representative image from which the pitch histogram in (e) was derived). g) Complementary secondary electron and energy dispersive spectroscopy (EDS) maps confirming the rivulets are nickel (*see Methods*). h) The equilibrium contact angle  $\theta_o$  between the final Ni nanoparticle and Si substrate surface was determined to be  $88^\circ \pm 5^\circ$  by image analysis of tilted SEM images following 20 pulses using  $E_d = 380\text{ mJ/cm}^2$ . i) The variation in the dewetted nanoparticle pitch mirrors the dispersion in the underlying modified, RP instability. The scale bars have deliberately been set to equal the fastest growing mode as predicted by LSA – the nanoparticle pitch closely reflects this value.

**Figure 2** The directed assembly of linear nanoparticle arrays was accomplished by prescribing a single synthetic varicose perturbation on the initial thin film strip. a) Varicose prescription effectively provides a “head start” for amplitude evolution for an unstable mode – larger amplitudes lead to a more rapid formation of nanoparticles. For example, the unstable mode shown ( $\lambda=1.96\mu\text{m}$ ) is still in the evolution phase for a synthetic perturbation of amplitude  $A_0=36\text{nm}$  while the equilibrium nanoparticle morphology has formed for the case of  $A_0=216\text{nm}$ . The experiments were conducted using a constant photon dose of 5 pulses at  $420\text{ mJ/cm}^2$ . b) Fast Fourier transforms (FFT) reveal the change from self- to directed-assembly with increasing initial amplitude. FFT’s calculated at  $A_0=0, 36, 44, 96, 126$  and  $196\text{ nm}$  reveal the emergence of a discrete peak at the synthetic wavelength ( $\sim 2\mu\text{m}$ ) with increasing  $A_0$ . A less intense, satellite peak emerges at  $\sim 1\mu\text{m}$  and is predicted by nonlinear hydrodynamic simulations (*see figure 4a later*). For clarity, the evolution of the Fourier components ( $A_n$ ) of the  $\sim 1$  &  $2\mu\text{m}$  modes as a function of initial varicose amplitude has been projected onto the  $\lambda=0\mu\text{m}$  plane in the figure as orange, hatched curves. c) The inset shows the Fourier spectra of the  $A_0=0\text{ nm}$  (self-assembly) and  $A_0=216\text{ nm}$  (directed-assembly) cases. The spectra have been normalized in order to highlight 1) the narrow and discrete nature of the synthetic Fourier mode for the directed-assembly case as well as 2) the similarity of the Fourier spectra, for the  $A_0=0\text{ nm}$  case, to the curve predicted by LSA of the modified RP model (revisit figure 1e), which is not surprising since the modes characterized by small growth rates lead to only small contribution to the FFT spectra.

**Figure 3** a) Synthetic modes were found to be either stable ( $\lambda=0.8\mu\text{m}$ ) or unstable ( $\lambda=1.352$  &  $2\mu\text{m}$ ) as predicted by LSA (5 laser pulses,  $E_d=420\text{ mJ/cm}^2$ ,  $w=2\mu\text{m}$  and  $h=23\text{nm}$ ). b) Nanoparticle formation, i.e., rivulet breakup, was accelerated with increasing initial synthetic amplitude. The amplitude, in nanometers, imposed at the edge of each Ni thin film strip is shown at the right of each SEM image. The same photon dose was used as in (a). c) The table shows a summary of the final Ni morphology as a function of initial synthetic wavelength and amplitude. The photon dose is the same as in b). The stable mode ( $\lambda=0.8\mu\text{m}$ ) decays back to the rivulet, without breakup, regardless of the magnitude of the initial amplitude. Among the unstable modes, the  $1.96\mu\text{m}$  mode forms nanoparticles more rapidly, for smaller magnitudes of  $A_0$ , when compared with the  $1.35\mu\text{m}$  mode since the growth rate for the  $1.96\mu\text{m}$  mode is greater (*see the LSA curve in figure 1e*). d) The natural instability begins evolving in the thin film strip, patterned with the  $820\text{nm}$  stable mode. A fluence of  $380\text{ mJ/cm}^2$  and 20 laser pulses was applied to the Ni thin film annulus patterned with the  $820\text{nm}$  stable varicose mode (falsely colored as green in the SEM overlay image collage). The  $820\text{nm}$  synthetic perturbation decayed during the 20 laser pulses followed by rivulet breakup leading to a particle spacing consistent with the fastest growing

unstable mode predicted by the modified Rayleigh–Plateau instability (blue, falsely colored SEM image) **S4**. In contrast, the unstable  $1.66\mu\text{m}$  mode yields a nanoparticle pitch consistent with the imposed synthetic perturbation for the same photon dose.

**Figure 4** Accurately and precisely defined nanoparticle arrays. The nanoparticle arrays were derived from 7 thin film strips originally oriented along the lateral dimension of the figure. PLiD was initiated using an energy density of  $400\text{mJ}/\text{cm}^2$  and 5 laser pulses. The starting thin film strip contained a sinusoidal synthetic perturbation with a  $720\text{nm}$  wavelength. The initial amplitude of the perturbation in the thin film strip was  $72\pm 24\text{nm}$ . The thin film strip height was  $23\pm 1.2\text{nm}$  and the average width of the strip was  $408\pm 24\text{nm}$ . The synthetic perturbation translated into an unstable varicose perturbation of the same wavelength in the intermediate rivulet. As a result, the final nanoparticle pitch was  $720\pm 48\text{nm}$  and the nanoparticle radius was  $142\pm 24\text{nm}$ .

**Figure 5** Nonlinear hydrodynamic simulations of  $2\mu\text{m}$  wide Ni thin film strips ( $h=23\text{nm}$ ) with an initial synthetic amplitude of  $A_0=108\text{nm}$ . The simulations were performed to emulate the experimental results shown in figure 3a. a) The synthetic perturbation characterized by  $\lambda=800\text{nm}$  decays and leads to a smooth and uniform rivulet on the time scale spanning  $200\text{ns}$ . In contrast, the perturbations characterized by  $\lambda=1352\&1960\text{nm}$  lead to the formation of nanoparticles during this timescale as seen in experiments. b) For longer times, the Ni thin film strip perturbed by the  $800\text{nm}$  edge mode breaks up into nanoparticles whose particle separation is much larger than the initially imposed wavelength. Similarly to the experiment for the  $\lambda=820\text{nm}$  case (strip width of  $2.4\mu\text{m}$ ) shown in figure 3d, a nanoparticle spacing consistent with the fastest growing mode sets the final nanoparticle pitch.